Isitman, Ogulcan; Kandemir, Hakan; Alcan, Gokhan; Cenev, Zoran; Zhou, Quan

Simultaneous and Independent Micromanipulation of Two Identical Particles with Robotic Electromagnetic Needles

Published in:
Proceedings of MARSS 2022 - 5th International Conference on Manipulation, Automation, and Robotics at Small Scales

DOI:
10.1109/MARSS55884.2022.9870468

Published: 01/01/2022

Document Version
Peer-reviewed accepted author manuscript, also known as Final accepted manuscript or Post-print

Please cite the original version:
Isitman, O., Kandemir, H., Alcan, G., Cenev, Z., & Zhou, Q. (2022). Simultaneous and Independent Micromanipulation of Two Identical Particles with Robotic Electromagnetic Needles. In S. Haliyo, M. Boudaoud, E. Diller, X. Liu, Y. Sun, & S. Fatikow (Eds.), *Proceedings of MARSS 2022 - 5th International Conference on Manipulation, Automation, and Robotics at Small Scales* (Proceedings of MARSS 2022 - 5th International Conference on Manipulation, Automation, and Robotics at Small Scales). IEEE.
https://doi.org/10.1109/MARSS55884.2022.9870468

Simultaneous and Independent Micromanipulation of Two Identical Particles with Robotic Electromagnetic Needles

Ogulcan Isitman[1], Hakan Kandemir[1], Gokhan Alcan[1], Zoran Cenev[2], Quan Zhou[1]

***Abstract*— Magnetic manipulation of particles at close vicinity is a challenging task. In this paper, we propose simultaneous and independent manipulation of two identical particles at close vicinity using two mobile robotic electromagnetic needles. We developed a neural network that can predict the magnetic flux density gradient for any given needle positions. Using the neural network, we developed a control algorithm to solve the optimal needle positions that generate the forces in the required directions while keeping a safe distance between the two needles and particles. We applied our method in five typical cases of simultaneous and independent microparticle manipulation, with the closest particle separation of 30 μm.**

I. Introduction

Manipulation at the microscale can be achieved using chemical [1], magnetic [2], optical [3], acoustic [4], and electrical [5] fields or a combination thereof [6]. Among those strategies, magnetic field-driven manipulation has drawn great attention due to its capability to remotely generate relatively strong torques and forces on magnetic materials in three dimensions [7]. Magnetic fields can also transmit safely into the biological tissues [8] and can exert motions in multiple degrees-of-freedom (DOF) on the micro agents [7]. Due to the size constraints, the capabilities of a single micro robotic agent are limited in terms of the payload, task speed, and complexities [9].

Numerous methods have been suggested to empower simultaneous and independent manipulation of multiple magnetic robotic agents. For most applications, these magnetic agents are located relatively far from multiple fixed magnetic sources and all the micro agents in the workspace receive the same magnetic fields [2]. Therefore, it is difficult to control the motion of multiple agents independently at the same time. To address this issue, researchers propose time-varying magnetic fields to exploit inhomogeneities in rotor axis orientation [10] or using micro agents with different resonant frequencies [11]. Methods using sequential pulses of different uniform magnetic fields [12] have also been proposed and shown very promising results. Alternatively, researchers used non-uniform field and gradient inhomogeneity for independent control in 2D [13] and 3D [14]. This technique allows manipulating of both identical and non-identical microrobots. A non-uniform field generator with a large field gradient is required in this method, which results in high currents and overheating. Among all those methods, the lack of localization of the field hinders the capability of the independent manipulation of the closely placed micro agents.

To increase the field gradient and localize the magnetic field electromagnetic needles with tapered magnetic poles have been proposed. This technique is especially useful in applications that require a high force [15], [16]. A robotic electromagnetic needle (REMN) is a promising magnetic field gradient-pulling technique with a mobile magnetic source that can selectively manipulate microparticles [17], [18]. Seon *et al.*, showed that a single REMN can achieve automatic non-contact manipulation by separating two adjacent particles, selective extraction of particles from a population, and sequential manipulation of four particles [19]. Those capabilities are extended to full plane control in our previous work by employing two cooperative REMNs [20].

In this work, we propose a simultaneous and independent manipulation method for two identical particles. Our method is based on the inhomogeneity of the magnetic field generated by the two mobile robotic electromagnetic needles. Compared to existing methods, the proposed technique generates a localized field to manipulate the particles in close vicinity and extend the capabilities of the robotic magnetic needles without hindering selectivity and high force capability. We carried out computer simulations to calculate the magnetic field in the workspace depending on the needle positions. Using the simulation data we train a neural network that makes fast and accurate predictions of magnetic field gradients which can be used to estimate the force on the particles based on given needle positions. Consequently, our control algorithm solves the optimal needle positions that generate the forces in the required directions while keeping a safe distance between the two needles and particles. We applied our method in five typical cases of simultaneous and independent microparticle manipulation, with the closest particle separation of 30 μm.

II. Materials and Methods

A. Concept of Magnetic Manipulation

The magnetic force acting on a single particle is a function of the particle magnetization and the magnetic field gradient [15]:

$$\mathbf{F} = \nabla(\mathbf{m}_p \cdot \mathbf{B}) \tag{1}$$

where $\mathbf{m_p}$ is the magnetic moment of a single particle, $\mathbf{B}$ the magnetic flux density. Note, in this paper, the bold symbols represent vectors.

*Research supported by Academy of Finland Project 331149 and 328239.

[1]Authors are with the Department of Electrical Engineering and Automation, School of Electrical Engineering, Aalto University, 00076, Aalto. Finland.

[2]Author is with the Department of Applied Physics, School of Science, Aalto University, 00076, Aalto. Finland.

All email addresses: firstname.lastname@aalto.fi.

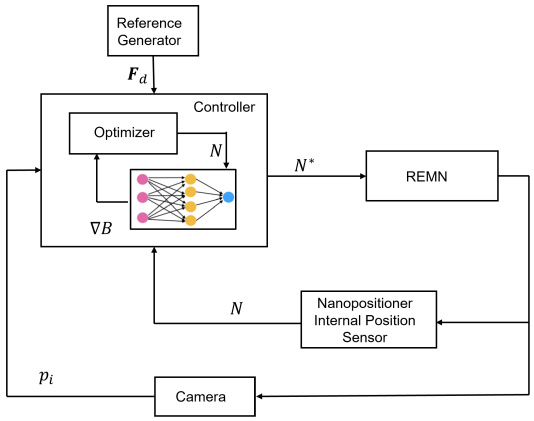

Fig. 1. Optimization-based controller approach

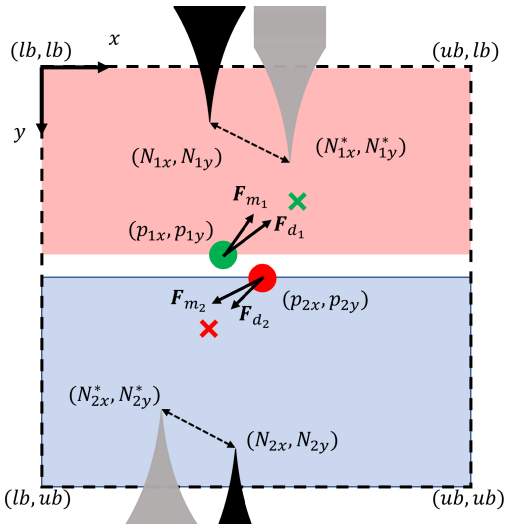

Fig. 2. Simultaneous and independent particle manipulation concept. The red cross represents the target position for the particle. (p_{1x}, p_{1y}) is the current position of the particle 1 (in green). The green cross represents the target position for the particle 2. (p_{2x}, p_{2y}) is the current position of the particle 2 (in red). $\mathbf{F}_{d_i}$ is the desired force vector and $\mathbf{F}_{m_i}$ is the modelled magnetic force which is a function of the gradient of magnetic flux density ∇B. The current needle positions (in black) are (N_{ix}, N_{iy}), the predicted optimal needle positions (in grey) are (N^*_{ix}, N^*_{iy}). lb and ub are the upper and lower boundary constraints, respectively.

An external magnetic field generates magnetic torque on the magnetic particles proportional to the field. Since the particles are free to rotate, the magnetization axis of the particles align with the field vector. Assuming the size of the particle is negligible compared to particle-needle distance and, the magnetic field is sufficiently high that the particle's magnetic moment is saturated, the magnetic force acting on a particle can be simplified as [21];

$$\mathbf{F}_m = m\nabla B = m\begin{bmatrix}\frac{\partial B}{\partial x} & \frac{\partial B}{\partial y} & \frac{\partial B}{\partial z}\end{bmatrix} \tag{2}$$

The magnetic moment of the superparamagnetic particle $\mathbf{m}_p$ reduces to m, which denotes the magnetic saturation of the particle. Equation (2) implies that provided the magnetic field and its gradient are known, the magnetic force on a particle can be calculated. The gradient of the magnetic flux density ∇B can be expressed for a parabolic-shaped pole tip as [16] ;

$$\nabla B = \frac{4\beta\mu_0 M_n}{(4\beta\delta + 1)^2} \tag{3}$$

where M_n is the needle core magnetization, which is a function of magnetic susceptibility of the material, number of turns per unit length, and applied current to the needle. β is the pole shape coefficient, δ is the distance between the particle and the tip needle.

Two REMNs generate an inhomogeneous magnetic field and the direct calculation of the spatial distribution of the field is not trivial due to the interaction of the needles. As a result, we employed finite element analysis (FEA) calculations to calculate the magnetic field and its gradient. Subsequently, we trained an artificial neural network to generalize the results and calculate the magnetic field for any point on the workspace and any given set of needle positions with a constant current.

B. Optimization and Controller

Our electromagnetic manipulator has two mobile needles. It is an over-actuated system for single-particle manipulation where there is no unique solution for the given task without introducing additional constraints, and simultaneous and independent manipulation of multiple particles poses additional challenges for designing a controller. We formulate the task as an optimization problem that results in needle positions that can generate desired magnetic field gradients on multiple particles. This is formulated as a constrained optimization problem given in (5).

The optimization-based manipulation scheme is given in Fig. 1., with a controller including an optimizer and a neural network model. The optimizer uses the cost function described in (5) to find the optimal needle positions. Calculations for the field are done by the neural network model, explained in Section II-D. The controller gets the desired force vector, $\mathbf{F}_{d_i}$ for $i \in \{1, 2\}$, considering the target position from a reference generator, and measurement of the particle positions $p_i \in R^2$ from camera and needle positions $N_i \in R^2$ from internal sensors of 3 DOF nanopositioner.

$$N = [N_{1x}\ N_{1y}\ N_{2x}\ N_{2y}\ ]^T \tag{4}$$

The input for the algorithm is the desired direction of the magnetic force, the current positions of the needles, and the particle positions. The output of the controller is the optimal needle positions, N^* which can be calculated by solving the following optimization problem:

$$\begin{aligned} \min_N \quad & \sum_{i=1}^{2} \|\mathbf{F}_{d_i} - \mathbf{F}_{m_i}(\nabla B)\| \\ \text{subject to} \quad & \nabla B = f(N, p_i), \\ & N_{lb} \le N \le N_{ub}, \\ & N_{lb} = [lb,\ lb,\ lb,\ \max(p_{1y}, p_{2y}) + \epsilon]^T, \\ & N_{ub} = [ub,\ \min(p_{1y}, p_{2y}) - \epsilon,\ ub,\ ub]^T, \end{aligned} \tag{5}$$

where $\|.\|$ is the Euclidean norm of a vector. The controller aims to find the optimal needle positions that minimize the difference between the magnetic force, $\mathbf{F}_{m_i}(\nabla B)$, and the desired force vector, $\mathbf{F}_{d_i}$, for each selected particle while avoiding potential collision of the needles. The magnetic flux density gradient, ∇B, is predicted by the function $f(.)$ which is modeled using neural network as explained in Section II-D. The term ϵ is added to y-direction boundaries to provide a distance margin between the needles to avoid collisions. Other variables are explained in Fig. 2.

C. Computer Simulations and Data Generation

We modeled the system in COMSOL Multiphysics 6.0. Our model solved the Maxwell equations in a 2D geometry. The geometry includes the surrounding air domain, water in the petri dish, needles, and coils. All required material properties are assigned to the corresponding domains, by using the built-in material library of the software. At the edges of the air domain, we inserted infinite element domains to represent continuity. Finally, to represent the needle geometry accurately, we interpolated the needle geometry by using microscopic images. The tip of the needle is expressed with a parametric curve, $y = 27x^2$. We used a constant input current of $0.25A$ for each needle, and each needle has the same polarization. We also performed a mesh convergence study to determine the optimal mesh size. The inputs for the simulations are the tip positions of the upper and lower needle: $N_{1x}, N_{1y}, N_{2x}, N_{2y}$. We solved the magnetic field for the input parameter ranges of -0.3 to 0.3 mm, each in 0.1 mm steps.

D. Neural Network Based Modeling

The proposed optimization-based controller approach (Fig. 1) requires information on the gradient of the magnetic flux density at the given points in the workspace, and for the given needle positions. It is possible to calculate the field in the whole workspace by using COMSOL; and for each case, solving the model takes less than 10 seconds. Albeit a fast solution, this speed of calculations is not useful for online optimization. Therefore, we used a neural network model to predict the gradient in the given points, i.e. at the locations of the particles, in the workspace. We utilized two separate two-layer fully-connected neural networks, shown in Fig. 3, to model the magnetic field gradient in the x and y directions. Our choice of the network architecture is inspired by the claim of Cybenko [22], that a neural network with only one hidden layer is always capable of approximating a multi-variant continuous function.

We performed a hyperparameter search study to determine the optimal size of the layers. The study first showed that a selection of a sufficiently high and equal number of units can provide promising prediction performances. Subsequently, we selected 128 unit numbers for both networks. The computer simulations also indicated that the magnetic field gradients are nonlinear fields. In order to represent the nonlinearity efficiently, we chose rectified linear units [23] as activation functions for hidden layers and linear functions

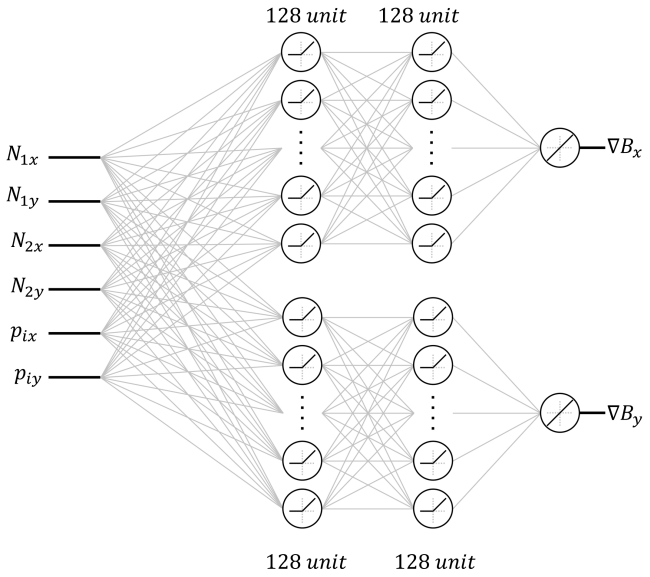

Fig. 3. Proposed two-layer neural network model for magnetic flux gradients

for the output layer. Computer simulations generated nearly 10.4 million samples, and 80% of those are used in training, with a mini-batch size of 64 samples. The remaining 20% of the data is used as the validation set. Finally, we used a stochastic optimizer, adaptive moment estimation [25] with a fixed learning rate of 0.001.

E. Experimental Setup

A robotic electromagnetic needle system, as shown in Fig. 4, was employed in simultaneous and independent micromanipulation experiments. The system consists of two identical 3-DOF electromagnetic needles. The diameter of the needles is 0.5 mm, the length is 21 mm, and the tip radius is around 15 μm. The needles are coiled with copper wire (AWG 34) for about 900 turns in 4 layers. Each of the 3-DOF nanopositioners is built from three identical stages (SLC1720, SmarACT, Germany) with sub-nanometer resolution and a maximum range of 12 mm.

The superparamagnetic microparticles are polystyrene encapsulated fluorescent iron-III-oxide (Fe_3O_4@PS, Microparticles Germany) with a 4.54 μm mean diameter and density of about 1.5 g/cc. Microparticles (10 μL of stock dispersion, particle concentration: 1% w/v) were diluted with

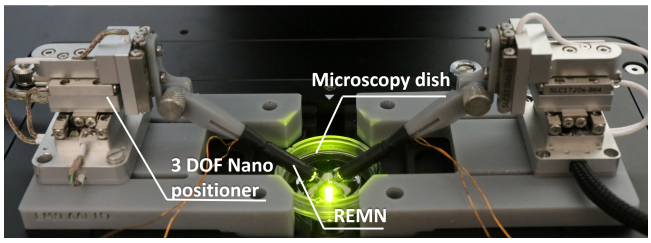

Fig. 4. The experimental setup is mounted on an inverted microscope. Two electromagnetic needles are positioned on separate 3-DOF nanopositioner.

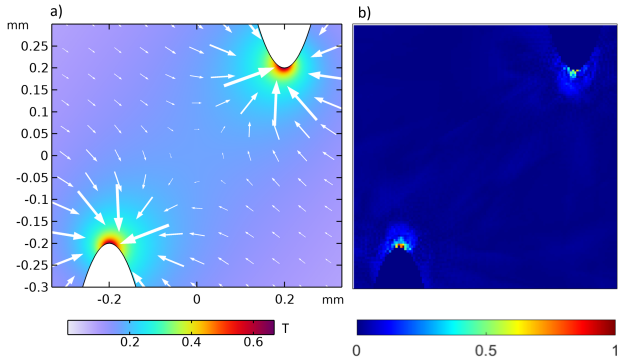

Fig. 5. a) COMSOL results of magnetic flux density norm (T) and its gradient. b) Normalized error between COMSOL simulations and trained neural network prediction for a given needle configuration.

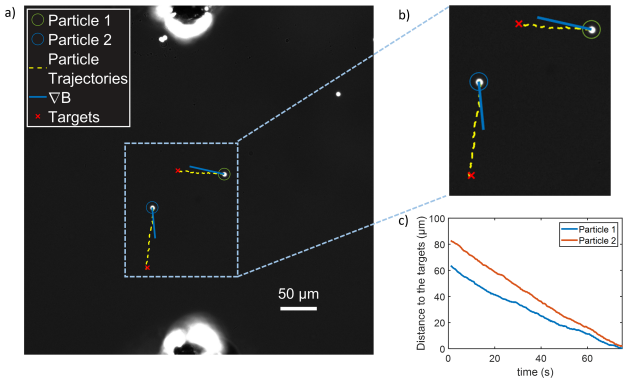

Fig. 6. a) Simultaneous and independent manipulation of two particles performing orthogonal motion with initial distance 30 μm. b) Close-up view of the particles. c) Euclidean distances between each particle and its target throughout their motion

100 mL of water (deionized Milli-Q). A dose of $\sim$10 μL solution has hundreds of microparticles within the sample carrier.

A video camera (Prime BSI, Teledyne Photometrics, USA) attached to an inverted microscope (Nikon Ti2-E, Japan) provides visual feedback. The workspace is observed with a dry objective (CFI Plan Apochromat 20X, N.A. 0.75 Nikon Ti2-E, Japan). The camera resolution is 2048px $\times$ 2048px pixels, and the resulting field of view is about 655 μm x 655 μm. A data acquisition device (NI 6343, National Instruments, USA) is used to control the electromagnetic needles, where the computer-generated signal is amplified by a current amplifier (TS200, Accel Instruments, USA). A constant current of 0.25 A is supplied to the needles unless they are turned off intentionally.

The optimization-based control is implemented using Python 3.9.2. The vision feedback algorithms are implemented using OpenCV-Python 4.5.1.48. The optimization is realized using SciPy 1.7.0 Nelder – Mead direct search method. Particle positions are obtained using the blob detection technique from the visual feedback [26].

III. Results and Discussion

A. Computer Simulations and Neural Network

We used the data generated by computer simulations to train the neural network. To measure the goodness of the fit between the simulated model responses and the measurement data, the fit metric is calculated as

$$fit = 100 \times \left(1 - \frac{\|y - \hat{y}\|}{\|y - \bar{y}\|}\right) \tag{6}$$

TABLE I
Training and Validation Accuracies of the Magnetic Gradient Models

	Training [%]	Validation [%]
∇B_x	83.36	83.50
∇B_y	82.76	82.68

where y is the measurements, $\hat{y}$ is the model predictions, and $\bar{y}$ is the mean of the measurements. Table 1 presents the training and validation accuracies using the fit metrics given above. Fig. 5 presents the magnetic flux density norm and its gradient for a given configuration of the needles and gives the error between the computer simulations and the neural network prediction. Large errors are observed especially in the vicinity of each needle. Our cases, however, have particles in the middle of the field where the error is negligible.

B. Experimental Demonstration of Typical Manipulation Cases

We selected 5 typical cases to demonstrate the capability of simultaneous and independent manipulation. These cases are i) orthogonal linear motion, ii) opposite linear motion, iii) opposite circular motion, iv) opposite parallel motion, and v) parallel motion. We believe most of complicated trajectory in 2D can be built by combining these typical cases.

Fig. 6a illustrates the first case, where two closely (30 μm) placed particles have been manipulated in orthogonal directions. Red crosses represent the targets for both particles and the yellow line represents their paths during the manipulation. Blue arrows show modeled field gradients on each particle due to the optimized needle positions. Fig. 6b shows the Euclidean distances between each particle and its target throughout their motion. Both particles move towards their targets simultaneously, and the slope of the graph represents the velocity of each particle. Mean velocity and the standard deviation (mean $\pm$ SD) of particle 1 and 2 are $1.03 \pm 0.27 \mu m/s$ and $1.13 \pm 0.35 \mu m/s$, respectively. The velocity of the second particle is higher under the optimal input conditions, it experiences a higher gradient. Our algorithm does not enforce the needles to be at equal distances to each particle, therefore the closer the particle to a needle, the higher the force it experiences. Furthermore, Fig. 5 implies that the gradient changes direction around the midpoint of the line connecting each needle. As a result, an orthogonal motion of particles in close proximity is only possible around the midpoint. The change in direction also

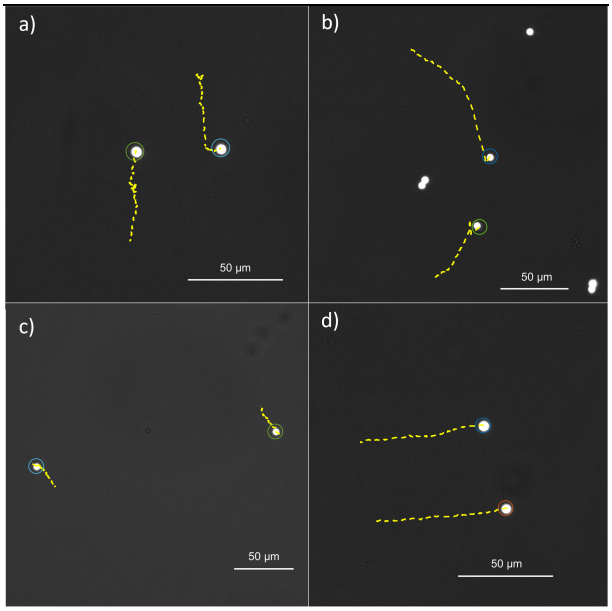

Fig. 7. Four cases of simultaneous and independent manipulation. a) Particles initially separated by 45μm are moved in opposite directions vertically. b) Particles initially separated by 54 μm are moved in circular trajectories. c) Particles initially separated by 210 μm are moved in opposite directions diagonally d) Particles initially separated by 45 μm are moved in parallel horizontally

results in lower amplitudes of gradient, especially in the horizontal direction. Thus, the vertical motion in this set is faster than the horizontal motion.

Fig. 7 demonstrates the remaining 4 typical cases. In Fig 7a, particles initially separated by 45 μm are moved in opposite directions vertically with the particle velocities of $0.99\pm0.19\mu m/s$ and $0.86\pm0.21\mu m/s$. Fig 7b represents the case of the circular motion, where the particles were initially separated by 54 μm and their velocities are $1.14\pm0.23\mu m/s$ and $1.61\pm0.85\mu m/s$. In Fig 7c relatively far (210 μm) particles move diagonally in opposite directions with the particle velocities of $0.84 \pm 0.39\mu m/s$ and $0.86 \pm 0.30\mu m/s$. In the last case particles initially separated by 45μm are moved in parallel horizontally having velocities of $1.28\pm0.5\mu m/s$ and $1.34 \pm 0.61\mu m/s$.

IV. Conclusions

In this study, we demonstrated a method for the simultaneous and independent manipulation of two particles at close vicinity. Using the simulation data we train a neural network that makes fast and accurate predictions of magnetic field gradients which can be used to estimate the force on the particles based on given needle positions. Consequently, our control algorithm solves the optimal needle positions that generate the forces in the required directions while keeping a safe distance between the two needles and particles. We applied our method in five typical cases of simultaneous and independent microparticle manipulation, with the closest particle separation of 30 μm. In 2D, more complex trajectories are possible as a combination of these typical cases. In the future, we are aiming to apply this methodology to first more complex trajectories and later to more particles.

References

[1] V. M. Fomin, M. Hippler, V. Magdanz, L. Soler,S. Sanchez, and O. G. Schmidt, "Propulsion mechanism of catalytic microjet Engines." *IEEE Transactions on Robotics*, 30(1), 40-48, 2013.

[2] M. P. Kummer, J. J. Abbott, B. E. Kratochvil, R. Borer, A. Sengul, and B. J. Nelson, "OctoMag: An electromagnetic system for 5-DOF wireless micromanipulation." *IEEE Transactions on Robotics*, 26(6), 1006-1017, 2010.

[3] X. Li, C. Liu, S. Chen, Y. Wang, S. H. Cheng, and D. Sun, "In Vivo Manipulation of Single Biological cells with an optical tweezers-based manipulator and a disturbance compensation controller." *IEEE Transactions on Robotics*, 33(5), 1200-1212, 2017.

[4] M. H. Kandemir, M. Beelen, R. M. Wagterveld, D. R. Yntema, and K. J. Keesman, "Dynamic acoustic fields for size selective particle separation on centimeter scale." *Journal of Sound and Vibration*, 490, 115723, 2021.

[5] R. L. Urbano, and A. M. Clyne, "An inverted dielectrophoretic device for analysis of attached single cell mechanics." *Lab on a Chip*, 16(3), 561-573, 2016.

[6] O. Youssefi, and E. Diller, "Contactless robotic micromanipulation in air using a magneto-acoustic system." *IEEE Robotics and Automation Letters*, 4(2), 1580-1586, 2019.

[7] M. Sitti, and D. S. Wiersma, "Pros and cons: Magnetic versus optical microrobots." *Advanced Materials*, 32(20), 1906766, 2020.

[8] J. J. Abbott, E. Diller, and A. J. Petruska, "Magnetic methods in robotics." *Annual Review of Control, Robotics, and Autonomous Systems*, 3, 57-90, 2020.

[9] S. Chowdhury, W. Jing, and D. J. Cappelleri, "Controlling multiple microrobots: recent progress and future challenges." *Journal of Micro-Bio Robotics*, 10(1), 1-11, 2015.

[10] A. Becker, O. Felfoul, and P. E. Dupont, "Simultaneously powering and controlling many actuators with a clinical MRI scanner." in *IEEE/RSJ International Conference on Intelligent Robots and Systems*, pp. 2017-2023, 2014.

[11] D. R. Frutiger, K. Vollmers, B. E. Kratochvil, and B. J. Nelson, "Small, fast, and under control: wireless resonant magnetic micro-agents." The International Journal of Robotics Research, 29(5), 613-636, 2010.

[12] M. Salehizadeh, and E. Diller, "Three-dimensional independent control of multiple magnetic microrobots via inter-agent forces." *The International Journal of Robotics Research*, 39(12), 1377-1396, 2020.

[13] D. Wong, E. B. Steager, and V. Kumar, "Independent control of identical magnetic robots in a plane." *IEEE Robotics and Automation Letters*, 1(1), 554-561, 2016.

[14] F. Ongaro, S. Pane, S. Scheggi, and S. Misra, "Design of an electromagnetic setup for independent three-dimensional control of pairs of identical and nonidentical microrobots." *IEEE transactions on robotics*, 35(1), 174-183, 2018.

[15] A. H. De Vries, B. E. Krenn, R. van Driel, and J. S. Kanger, "Micro magnetic tweezers for nanomanipulation inside live cells." *Biophysical journal*, 88(3), 2137-2144, 2005.

[16] X. Wang *et al.*, "Intracellular manipulation and measurement with multipole magnetic tweezers." *Science robotics*, 4(28), 2019.

[17] H. H. See, S. C. Herath, Y. Du, H. Asada, and P. C. Chen, "Localized manipulation of magnetic particles in an ensemble." *IEEE Access*, 6, 24075-24088, 2018.

[18] Z. Cenev, H. Zhang, V. Sariola, A. Rahikkala, D. Liu, H. A. Santos, and Q. Zhou, Q. "Manipulating superparamagnetic microparticles with an electromagnetic needle." *Advanced Materials Technologies*, 3(1), 1700177, 2018.

[19] J. A. Seon, Z. Cenev, and Q. Zhou, "Automatic noncontact extraction and independent manipulation of magnetic particles using electromagnetic needle." *IEEE/ASME Transactions on Mechatronics*, 25(2), 931-941, 2019.

[20] O. Isitman, H. Bettahar, Q. Zhou, "Non-Contact Cooperative Manipulation of Magnetic Microparticles Using Two Robotic Electromagnetic Needles." *IEEE Robotics and Automation Letters*, 7(2), 1605-1611, 2021.

[21] M. Stern, M. Cohen, and A. Danielli, "Configuration and design of electromagnets for rapid and precise manipulation of magnetic beads in biosensing applications." *Micromachines*, 10(11), 784, 2019.

[22] G. Cybenko, "Approximation by superpositions of a sigmoidal function." *Mathematics of control, signals and systems*, 2(4), 303-314, 1989.
[23] I. Goodfellow, Y. Bengio, and A. Courville, *Deep learning*. MIT press, 2016.
[24] D. P. Kingma, and J. Ba, "Adam: A method for stochastic optimization." *arXiv:1412.6980*, 2014.
[25] G. Alcan, M. Ghorbani, A. Kosar, and M. Unel, "A new visual tracking method for the analysis and characterization of jet flow." *Flow Measurement and Instrumentation*, 51, 55-67, 2016.